Available online at www.sciencedirect.com
ScienceDirect
Trans. Nonferrous Met. Soc. China 34(2024) 2918−2927
Transactions of Nonferrous Metals Society of China
www.tnmsc.cn

Formation mechanism of nanopores in dense films of anodic alumina

Peng-ze LI[1], Yu ZHANG[1], Jia-zheng ZHANG[2], Lin LIU[2], Shi-yi WANG[1], Rui LIU[1], Ye SONG[1], Xu-fei ZHU[1]

1. Key Laboratory of Soft Chemistry and Functional Materials of Education Ministry,
Nanjing University of Science and Technology, Nanjing 210094, China;
2. School of Environmental and Chemical Engineering, Jiangsu Ocean University, Lianyungang 222005, China

Received 27 February 2023; accepted 9 November 2023

Abstract: Constant-current anodization of pure aluminum was carried out in non-corrosive capacitor working electrolytes to study the formation mechanism of nanopores in the anodic oxide films. Through comparative experiments, nanopores are found in the anodic films formed in the electrolytes after high-temperature storage (HTS) at 130 °C for 240 h. A comparison of the voltage−time curves suggests that the formation of nanopores results from the decrease in formation efficiency of anodic oxide films rather than the corrosion of the electrolytes. FT-IR and UV spectra analysis shows that carboxylate and ethylene glycol in electrolytes can easily react by esterification at high temperatures. Combining the electronic current theory and oxygen bubble mold effect, the change in electrolyte composition could increase the electronic current in the anodizing process. The electronic current decreases the formation efficiency of anodic oxide films, and oxygen bubbles accompanying electronic current lead to the formation of nanopores in the dense films. The continuous electronic current and oxygen bubbles are the prerequisites for the formation of porous anodic oxides rather than the traditional field-assisted dissolution model.

Key words: anodic alumina; formation mechanism; nanopores; formation efficiency; electronic current; oxygen bubble

---

1 Introduction

It is well-known that aluminum and titanium can be anodized to obtain two kinds of anodic oxide films. One is a dense film, and the other is a porous film [1−3]. In recent years, porous anodic alumina (PAA) and anodic TiO_2 nanotubes (ATNTs) have received significant attention in various applications, such as solar cells, supercapacitors, and sensors [4−8]. However, the formation mechanism of nanopores or nanotubes in anodic oxides is still controversial. At present, popular formation mechanisms of the nanopores are field-assisted dissolution and field-assisted ejection models [9,10], oxide hydrolysis and equifield strength models [11,12], viscous flow and stress−strain models [13,14], and oxygen bubble mold effect [15−18]. The debate over these models is about the formation of initial nanopores in anodic oxides. The field-assisted dissolution model suggests that porous channels are dug “from top to bottom” by the dissolution digging. For example, PAA is generally prepared in oxalic acid, phosphoric acid, and sulfuric acid solution. In this case, the field-assisted dissolution reaction is expressed as $Al_2O_3+6H^+=2Al^{3+}+3H_2O$ [8]. Similarly, ATNTs are formed in the solution containing F^-; the field-assisted dissolution reaction of ATNTs is expressed as $TiO_2+6F^-+4H^+=[TiF_6]^{2-}+2H_2O$ [1,9,12]. However, viscous flow and oxygen bubble mold effect suggest that the nanopores in PAA and ATNTs grow “from the bottom up” [13−16]. So, how exactly are the nanopores in PAA and ATNTs formed? Do they grow according to the “digging

---

Corresponding author: Lin LIU, Tel: +86-18905131836, E-mail: liulin@jou.edu.cn;
Xu-fei ZHU, Tel: +86-13605167687, E-mail: zhuxufei.njust@vip.163.com

DOI: 10.1016/S1003-6326(24)66585-4

from top to bottom” manner or the “from the bottom up” described by the oxygen bubble mold effect? These findings presented in this work will provide a new interpretation of the above two opposed growing patterns.

Compared to PAA, there has been relatively less research on dense films of anodic alumina. Dense films are mainly used for corrosion protection of metals and as dielectric films in electrolytic capacitors [19−23]. The working electrolyte is required to have no corrosive effect on the dense film to improve the load life of aluminum electrolytic capacitors at high temperatures. Otherwise, due to the degradation of the dielectric properties of dense films, the life of the aluminum electrolytic capacitor will not reach the requirement of 3000 h at 125 °C. Recently, pure aluminum was anodized in the neutral and non-corrosive electrolytes, and many nanopores were found in the dense films. However, the formation of these nanopores cannot be explained by the field-assisted dissolution model mentioned above. Here, the formation mechanism of these nanopores in dense films of anodic alumina formed in the working electrolyte of capacitors was discussed to provide insights into the formation mechanism of porous anodic oxides.

2 Experimental

The sparking voltage of each electrolyte was tested to study the endurance voltage and breakdown characteristics of organic electrolytes in electrolytic capacitors. The testing method was to anodize pure aluminum at constant current. The primary purpose was to observe variations in the voltage−time curves of aluminum sheets in constant-current anodization and explore the anodization of pure aluminum in a given electrolyte, explicitly focusing on the sparking voltage.

2.1 Pretreatment of aluminum sheets

In this work, aluminum foil (purity, 99.999%, Baoji Titanium Tungsten Metal Limited Company), 200 μm in thickness, was used as the anode material, and the cathode material was a 10 cm × 1.3 cm × 0.2 cm graphite sheet. Before the anodization, aluminum foil was cut into 1 cm × 8 cm and electropolished in a mixed perchloric acid and ethanol (1:4 in volume ratio) at a constant current density of 300 mA/cm^2 for 60 s. After being polished, the samples were thoroughly rinsed with plenty of deionized water and air-dried under ambient conditions.

2.2 Preparation of organic electrolytes

This work focused on the anodization of pure aluminum in four electrolytes. Four electrolytes were neutral, which means they do not have any corrosion. The purity of chemicals used in the four electrolytes was capacitance grade.

The first electrolyte consisted of 4 wt.% 24-carbon multibranched tetrameric ammonium carboxylate (HS-01), 94 wt.% ethylene glycol (EG), and no more than 2 wt.% monobutylphosphate (MBP). The solute and solvent were mixed according to the specified ratio and then heated to 130 °C while continuously stirring until the solute was completely dissolved. Subsequently, MBP was added to the solution, and stirring continued at 130 °C until fully dissolved. The final mixed solution appeared to be transparent and stable. 500 g of the prepared mixed solution was used as the first electrolyte. The conductivity of the first electrolyte was 1320 μS/cm at 30 °C, measured by Shanghai LEI CI (DDSJ−307F) conductivity meter, and the pH was 6.8 measured by METTLER TOLEDO pH meter. The conductivity and pH of the following electrolytes were measured using the same methods as the first electrolyte.

The high-temperature stability of the first electrolyte was studied to optimize the capacitors’ performance. 200 g of the first electrolyte was stored in a sealed container at 130 °C for 240 h. The stored electrolyte was called the second electrolyte. The conductivity of the second electrolyte was 1108 μS/cm at 30 °C, and the pH was 6.7.

The third electrolyte consisted of 4 wt.% ammonium sebacate ($C_{10}H_{24}N_2O_4$), 84 wt.% EG, 10 wt.% polyethylene glycol (PEG) (relative molecular mass of PEG is 600), and no more than 2wt% MBP. The preparation method for the third electrolyte was the same as that for the first. The conductivity of the third electrolyte was 1560 μS/cm at 30 °C, and the pH was 6.8.

Similarly, the third electrolyte was stored in the same condition as the first, and the stored electrolyte was called the fourth electrolyte. The conductivity of the fourth electrolyte was

1248 μS/cm at 30 °C, and the pH was 6.7.

For studying the high-temperature stability and the changes in the composition of electrolytes after high-temperature storage (HTS), the electrolytes before and after storage were characterized by Fourier transform infrared (FT-IR) and UV spectroscopy. FT-IR spectra were obtained using a spectrophotometer (NICOLETIS10), covering 4000−500 cm^{-1} range. UV spectra were obtained using a spectrophotometer (UV−2200 spectrophotometer), covering the range of 200−800 nm, with deionized water serving as a reference solution.

2.3 Anodization

The whole anodizing process for testing the sparking voltage was carried out in the corresponding electrolyte at constant current (20 mA), room temperature, and normal air pressure. Voltage−time curves were automatically recorded by a computerized test system (H-1TV/3TV-C-Endurance Voltage Intelligent Tester). Once each electrolyte reached the sparking voltage, the anodizing duration was maintained for another 100 s. The anodization in each electrolyte was repeated three times, and the three voltage−time curves were almost identical. Samples with good repeatability were selected for the characterization of FESEM. To ensure that the cross-section of anodic oxide films can be seen, each sample needed to be artificially bent into the "Ω"-shape during the FESEM sample preparation [1].

3 Results and discussion

3.1 Anodization behavior of pure aluminum in the first and second electrolytes

Figure 1 shows FESEM images of the utterly dense film of anodic alumina anodized in the first electrolyte. No nanopores can be found on the surface (Figs. 1(a, b)) and the cross-section of the dense film (Fig. 1(c)), which suggests that the first electrolyte has no corrosive effect on the dense film. According to the field-assisted dissolution model, if the electrolyte was corrosive, there would be cracks or nanopores on the surface of the dense film [2,12]. Figure 1(d) shows the voltage−time curve of the constant-current anodization. Before reaching the sparking voltage, the curve appears almost as a straight line as the thickness of the anodic oxide film increases. This means that the slope of the curve is constant, which is approximately 1.48. The constant slope indicates that the total current of 20 mA is wholly used for the growth of the dense film, which means that the formation efficiency of the dense film of anodic oxides is almost 100% in Fig. 1 [16].

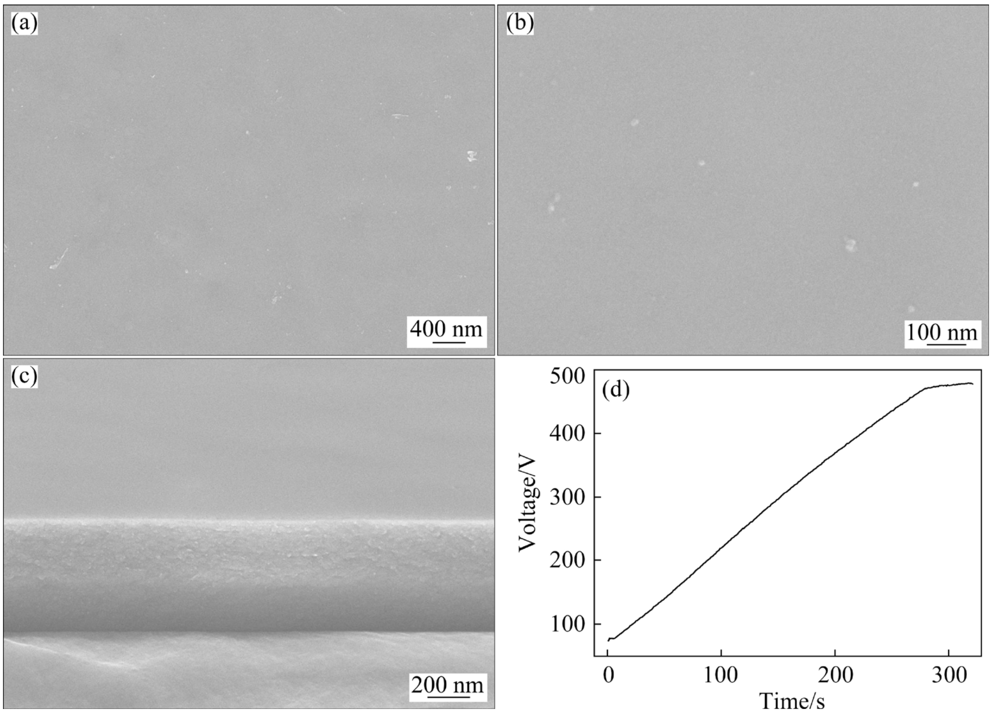

Fig. 1 FESEM images showing surface (a, b) and cross-section (c) morphologies of dense film anodized in the first electrolyte, and corresponding voltage−time curve (d)

Figure 2 shows FESEM images of the dense film of anodic alumina anodized in the second electrolyte. Figures 2(a, b) show SEM images of surface of the dense film, where no cracks and nanopores can be found on the surface. However, compared with Fig. 1(c), a clear "sandwich" structure appears in Fig. 2(c). In the "sandwich" structure, the upper and lower layers are dense films, with a clear, loose layer in the middle. There are several obvious cavities in the loose layer. The field-assisted dissolution model cannot explain the cavities of the loose layer because no nanopores can be seen on the surface in Figs. 2(a, b). It means that this electrolyte has no corrosive effect on the dense film.

The formation of cavities and the loose layer can only be discussed from the voltage−time curve, which can reflect the whole anodizing process. Compared to the curve in Fig. 1(d), Fig. 2(d) shows a clear inflection point (*E*) around 180 V. After the inflection point *E*, the formation efficiency of anodic oxides starts to decrease. For example, at 200 s, the voltage reaches about 308 V in Fig. 1(d), while in Fig. 2(d), it only reaches about 250 V simultaneously. Furthermore, the average slope in Fig. 2(d) is lower than that in Fig. 1(d), indicating that the formation efficiency in Fig. 2 is significantly lower than in Fig. 1 in the anodizing process. This may be due to the decrease in the oxidation efficiency of the electrolyte after 240 h of storage at 130 °C. Figure 3 shows the FT-IR and UV spectra of the first and second electrolytes. In Fig. 3, the peak at 1563.8 $\mathrm{cm^{-1}}$ should be the absorption peak of $\mathrm{COO^-}$ in HS-01, which disappears after HTS, while a new absorption peak appears at 1666.87 $\mathrm{cm^{-1}}$. In the UV spectra of Fig. 3(b), the $\mathrm{COO^-}$ has the maximum peak absorbance at 255 nm. However, after the HTS of the first electrolyte, it has a new peak absorbance at 344 nm. The new peaks at 1666.87 $\mathrm{cm^{-1}}$ and 344 nm in Fig. 3 are more likely to be the absorption peak of the ester bond generated by the reaction of carboxylate and EG. This change in electrolyte composition after HTS may lead to a decrease in oxidation efficiency. While the oxidation efficiency of electrolytes decreases after HTS, the sparking voltage of the second electrolyte is higher than that of the first electrolyte because of the decrease in the electrolyte conductivity from 1320 to 1108 μS/cm after storage at 130 °C.

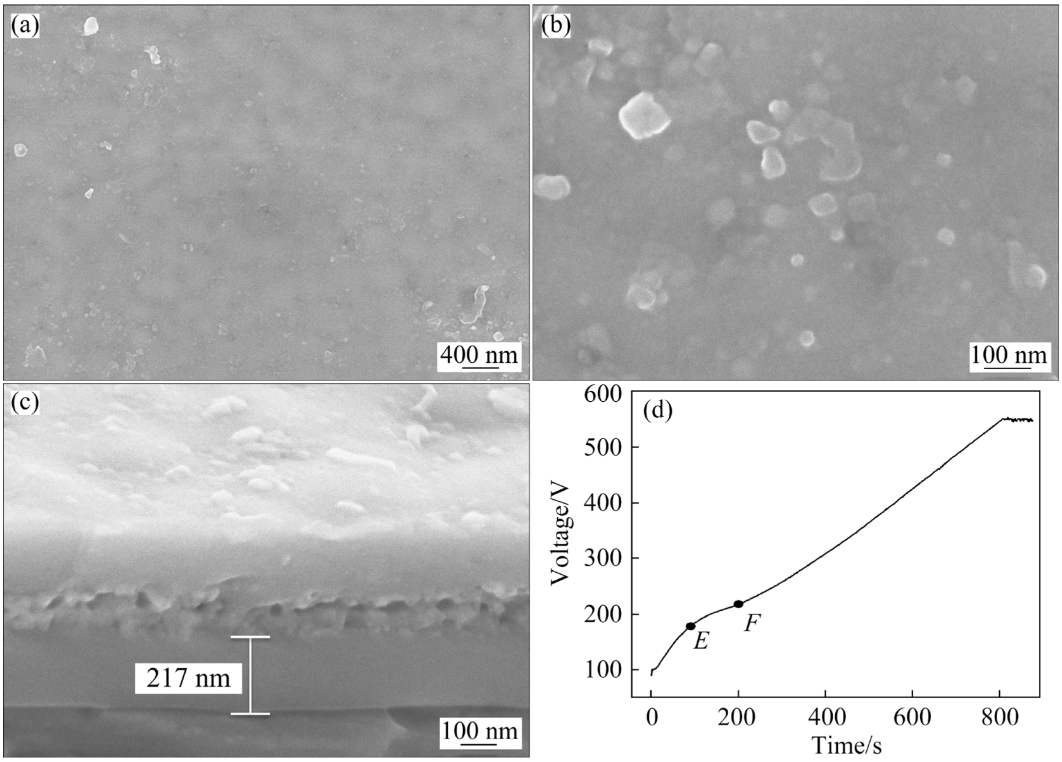

Fig. 2 FESEM images showing surface (a, b) and cross-section (c) morphologies of dense film anodized in the second electrolyte, and corresponding voltage−time curve (d)

3.2 Anodization behavior of pure aluminum in the third and fourth electrolytes

To further explore why the oxidation and the formation efficiency of anodic oxide differ for the same electrolyte (Fig. 1(d) and Fig. 2(d)) at the same anodizing current, the third and fourth electrolytes are compared next. The FESEM images of the surface and cross-section of the anodic oxide films anodized in the third and fourth electrolytes are shown in Fig. 4 and Fig. 5, respectively.

The third electrolyte containing ammonium sebacate as the main solute differs from the previous two electrolytes. However, its pH is still close to neutral, indicating that the corrosive effect of the third electrolyte is also weak. However, many nanopores are found in the anodic oxide film formed in the third electrolyte. In Fig. 4(a), there are a few concaves on the surface. Cavities with diameters of about 100 and 300 nm can be found in the cross-section of the anodic film in Figs. 4(b, c). The concaves on the surface and cavities on the cross-section are not always connected. For example, the right-most cavity in Fig. 4(c), with a diameter of about 300 nm, has no direct connection to the surface concave. The field-assisted dissolution reaction does not cause the cavities in Fig. 4 because the third electrolyte is almost non-corrosive. The voltage−time curves in Fig. 2(d)

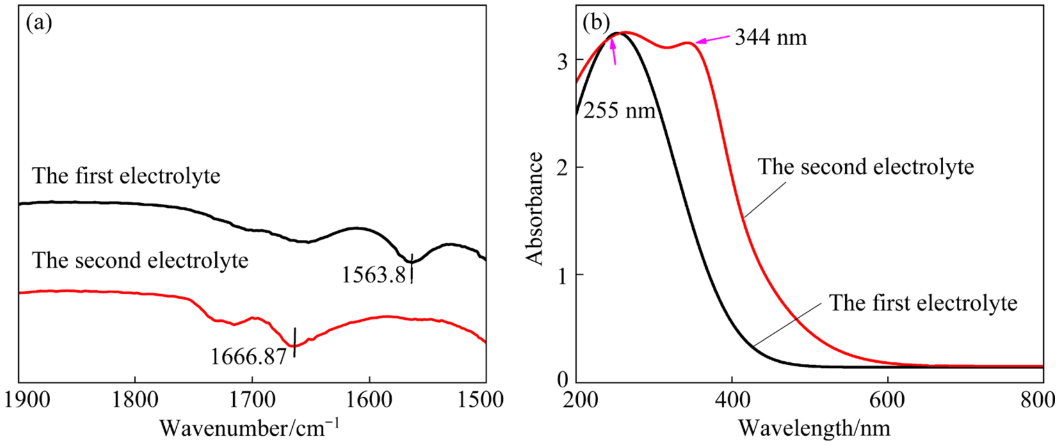

Fig. 3 FT-IR (a) and UV (b) spectra of the first and second electrolytes

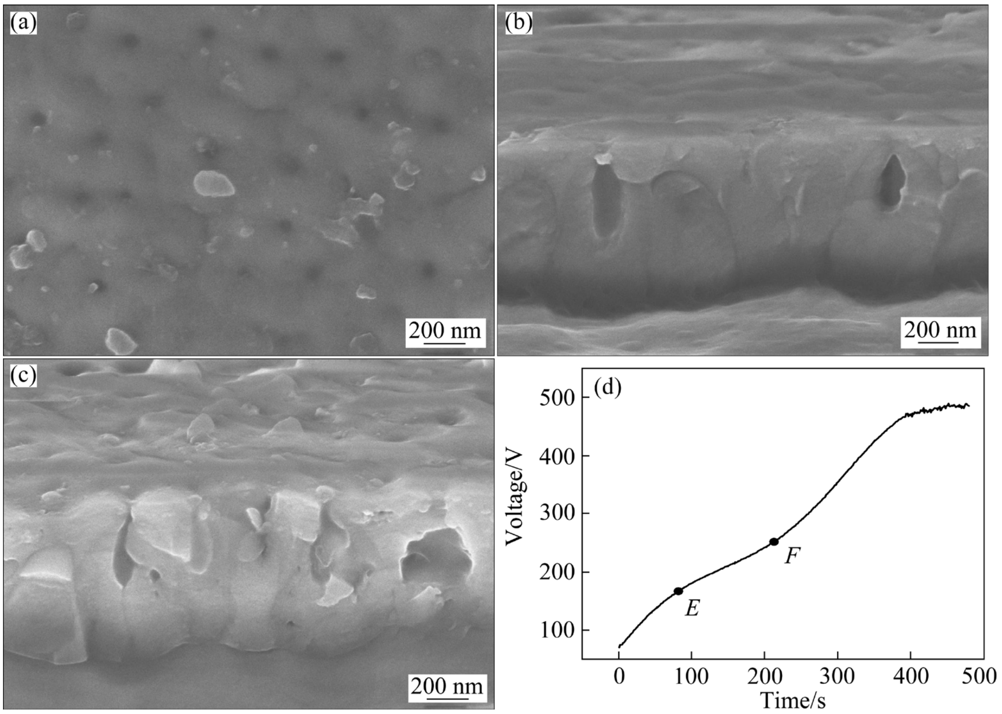

Fig. 4 FESEM images showing surface (a) and cross-section (b, c) morphologies of dense film anodized for about 490 s in the third electrolyte, and corresponding voltage−time curve (d)

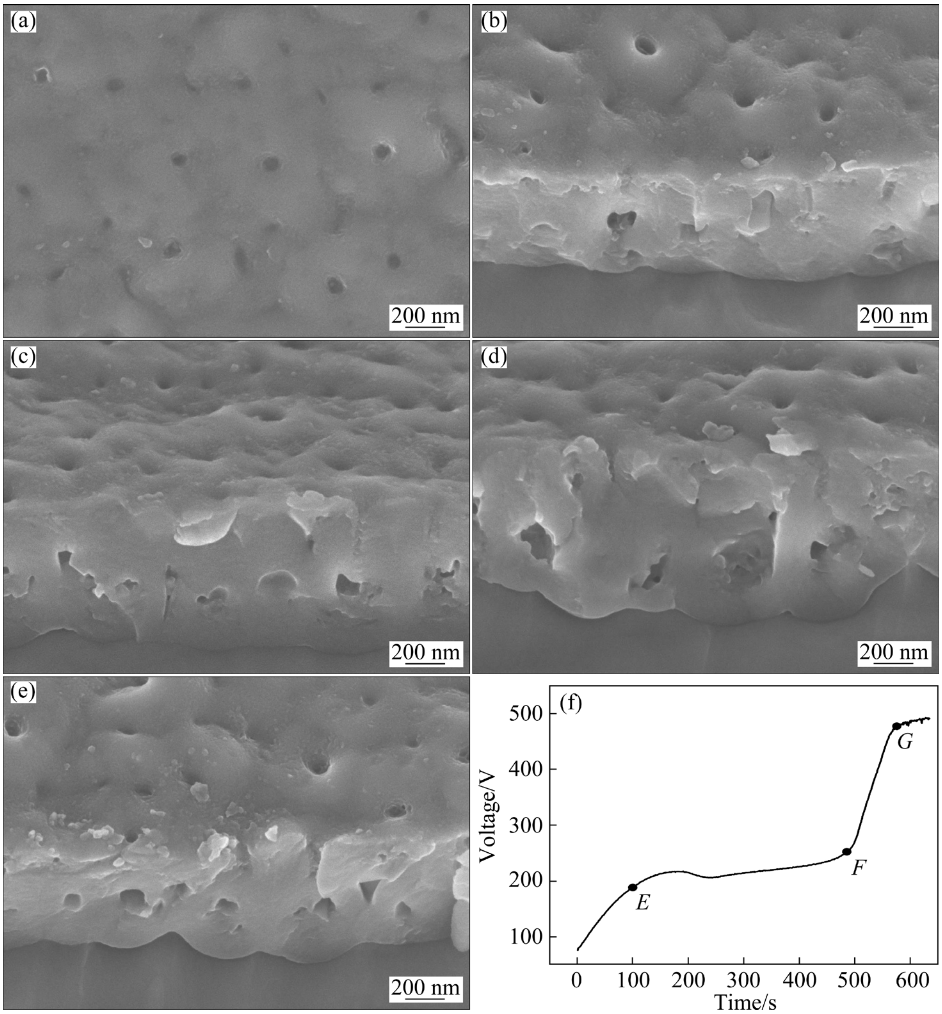

Fig. 5 FESEM images showing surface (a) and cross-section (b−e) morphologies of dense film anodized in the fourth electrolyte, and corresponding voltage−time curve (f)

and Fig. 4(d) have similar shapes. In Fig. 4(d), the voltage keeps rising with time until the sparking occurs at 466 V and about 400 s. This work artificially maintains the sparking duration for about 100 s. When the sparking occurs, gas and smoke are released from the surface of the anodic oxide film. Within this time, the endurance voltage of the film reaches its highest point, approximately 466 V, and then fluctuates up and down at 466 V [22−25]. After the sparking, the electrical breakdown of the film occurs, and the total current (I_T) of 20 mA in the anodizing process is completely transformed into the electronic current (I_e), which leads to the evolution of large amount of oxygen gas ($4OH^- = O_2\uparrow + 2H_2O + 4e$). That is, the applied electric field directly causes the release of electrons from the hydroxide ion into oxygen to maintain the source of many electrons in the electronic current at the breakdown state [26]. The most important concern is that the film thickness no longer increases within the 100 s duration after sparking, which means the formation efficiency of anodic oxides (η) decreases to 0. Therefore, in the growth process of anodic oxides, I_T consists of ionic current (I_{ion}) and I_e, $I_T=I_{ion}+I_e$. $I_{ion}=A\exp(BU_{app}/d)$ and $I_e=I_0\exp(\alpha d)$, it is clear that I_{ion} and I_e are both related to the thickness (d) of the barrier layer. A and B are temperature-dependent constants, E is the field strength ($E=U_O/d$), and U_O is the voltage across the barrier oxide. α is the impact ionization coefficient of the avalanche, and I_0 is the primary electronic current. In the anodizing process, I_{ion} is used to grow anodic oxides, and I_e leads to oxygen gas evolution [16−18]. At the beginning of the anodizing process, I_{ion} is completely used for the oxide growth. Thus, the η can be expressed as

$\eta=I_{ion}/I_T=100\%$. However, when the sparking occurs, the thickness of the anodic oxide film no longer increases, and the electrical breakdown occurs. I_T is completely transformed into I_e. Therefore, the η tends to be 0. So $\eta=I_{ion}/I_T=0$, that is $I_{ion}=0$ and $I_T=I_e$ [16,17].

Based on the above, we can analyze the voltage−time curve in Fig. 1(d). Since the slope of the curve has barely decreased, the η is almost 100%. Therefore, the voltage keeps rising with time until the sparking occurs. It can be considered that when the voltage keeps rising, there is almost no I_e, so η remains constant. In Fig. 2(d) and Fig. 4(d), after the inflection point E, the I_e, which does not form anodic oxides, starts to appear. The generation of I_e is the essential reason why η decreases in non-corrosive electrolytes. I_e leads to the oxygen gas evolution within the anodic oxides. However, due to the pressure of the atmosphere and the electrolyte, the oxygen bubbles which try to evolve cannot spill out beyond the anodic oxides, thus forming a loose layer in Fig. 2(c) and cavities in Fig. 4(c). After the inflection point E, as I_e begins to appear, the growth of anodic oxides and oxygen gas evolution are simultaneous. However, the I_e/I_T is smaller than I_{ion}/I_T, which allows new anodic oxides to cross over the oxygen bubbles and continue to grow on top of them. When the I_{ion} is dominant, the "sandwich" structure shown in Fig. 2(c) is formed. The loose layer in the middle of Fig. 2(c) is completed around 100 s after the inflection point E (EF period in Fig. 2(d)). Later, the slope of the voltage−time curve increases again, leading to the formation of dense films of anodic oxides in the top and bottom layers in Fig. 2(c). It has been documented that the newly anodic oxides grow simultaneously at the electrolyte/oxide and the oxide/Al interfaces. Compared to Fig. 2(d), it is clear that the EF period in Fig. 4(d) becomes a larger proportion of the total anodizing time. Therefore, the time of oxygen production is longer, resulting in more cavities in Figs. 4(b, c).

It should be pointed out that no dissolution current is contributed by the chemical dissolution reaction ($Al_2O_3+6H^+=2Al^{3+}+3H_2O$) in the anodizing process. Because the dissolution reaction only occurs at the electrolyte/oxide interface, there are no ions or electrons across anodic oxides [27]. Many research groups have shown that the dissolution of anodic oxides by the electrolyte is very weak [28−32], so the dissolution current can be ignored. It is the prerequisite for estimating the η by I_{ion} and I_e. The growth of the significant nanopores subsequently proceeds mainly due to the field-assisted flow of oxides rather than field-assisted dissolution [28,29]. Some researchers have reported that the formation of nanopores or nanotubes in anodic oxides of various metals is closely related to the oxygen gas evolution in the anodizing process.

According to the above, it is easier to understand that, in Fig. 5(f), the decreased η of the EF period is due to the generation of I_e and oxygen gas evolution. FESEM images in Fig. 5(a) to Fig. 5(e) show many surface concaves and cross-section cavities. The fourth electrolyte is still neutral and non-corrosive. The oxidation efficiency of the ammonium sebacate-based electrolyte is significantly decreased because I_e is more easily generated after 240 h of storage at 130 °C.

Figure 6 shows the FT-IR and UV spectra of the third and fourth electrolytes. Consistent with the result in Fig. 3(a), the absorption peak at around 1563 cm^{-1} disappears after the HTS of the

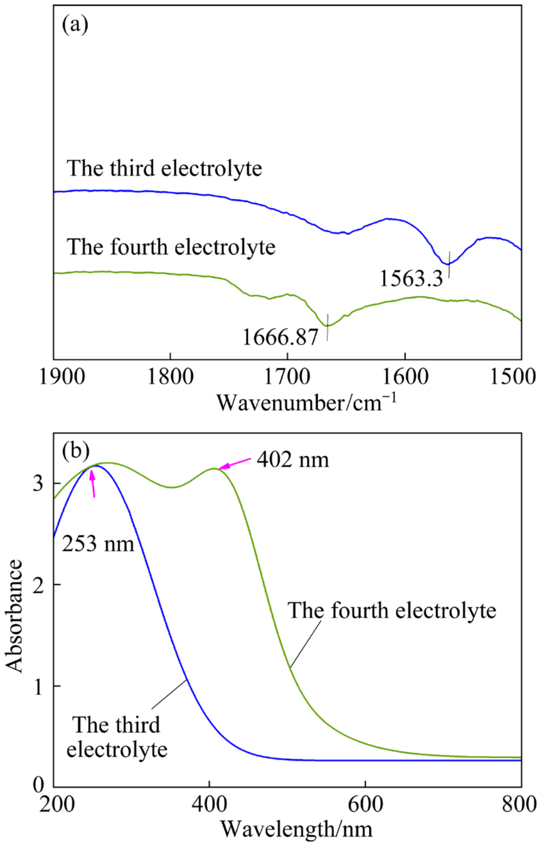

Fig. 6 FT-IR (a) and UV (b) spectra of the third and fourth electrolytes

third electrolyte while the absorption peak at around 1666 cm^{-1} appears in Fig. 6(a). In Fig. 6(b), it has a new peak absorbance at 402 nm. So, it can be inferred that when the electrolyte is at high temperatures, the carboxylate is likely to react with EG, which is the most common reason for the failure of working electrolytes in capacitors under high-temperature conditions.

3.3 Relationship between nanopores formation and electrolytes

In the anodizing process, the carboxylate in the organic electrolytes acts as solutes to provide O^{2-} for the formation of anodic oxides. After HTS, the ability of the electrolytes to provide O^{2-} is decreased because of the esterification reaction, which leads to a decrease in oxidation efficiency. The essence is also that the degradation of electrolyte performance leads to the generation of more electronic current and a decrease in the oxidation efficiency of electrolytes. In Fig. 5, the generation of I_e in the EF period leads to oxygen gas evolution. These evolved oxygen bubbles form the cavities within the anodic oxides in Fig. 5(e). The hemispherical arc at the bottom of the cavities in Fig. 5(e) proves that it is caused by the oxygen bubble mold effect [15,16]. The sparking voltage of the anodic oxide film in Fig. 5 is also about 490 V, which indicates that the overlying anodic oxides above the cavities seen in Fig. 5(e) grow in the FG period of Fig. 5(f). Therefore, the endurance voltage of the whole film can reach about 490 V. And during the formation of the completely dense film at constant current, the voltage−time curves can represent the formation efficiency of anodic oxides. However, nanopores are generated in the anodizing process. In that case, the rate of voltage rise per unit time changes, and an inflection point in Fig. 2(d) and 4(d) or a voltage plateau in Fig. 5(f) appears in the voltage−time curves. It means that the formation of the dense film is influenced by the nanopores, resulting in a change in the thickness of the dense film, so the voltage−time curve is also changing [15−18].

Figure 7 shows the surface and cross-section morphologies of the dense film of anodic alumina anodized in the third electrolyte. Differently from Fig. 4, the dense film in Fig. 7 forms when the electrolyte reaches the sparking voltage and stops immediately instead of maintaining it for 100 s. It can be seen that nanopores can also be found on the surface and cross-section of the dense film. The electronic current and oxygen bubbles are generated in the early stage of the dense film formation, which results in the generation of nanopores.

Table 1 shows a summary of the composition

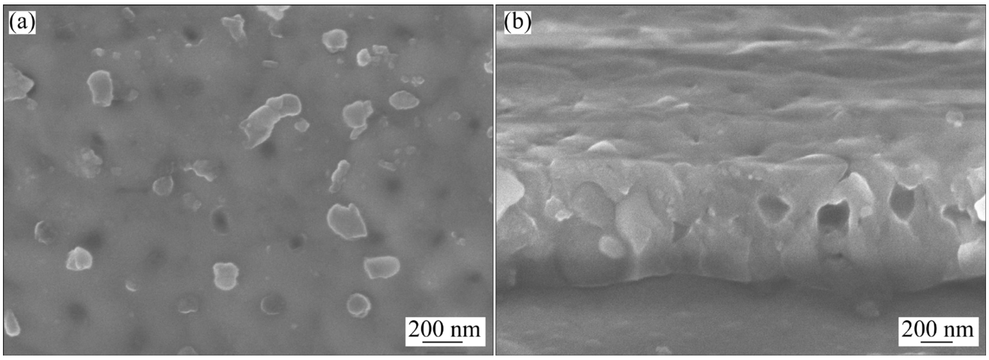

Fig. 7 FESEM images showing surface (a) and cross-section (b) morphologies of dense film anodized for about 390 s in the third electrolyte

Table 1 Summary of properties of four electrolytes

Electrolyte	Composition	Conductivity at 30 °C/(μS·cm^{-1})	pH	Sparking voltage/V	Morphology of anodic film
The first	4 wt.% HS-01+94 wt.% EG+2 wt.% MBP	1320	6.8	475	Completely dense film
The second	Same as the first but with carboxylic acid ester	1108	6.7	550	Sandwich structure
The third	4 wt.% $C_{10}H_{24}N_2O_4$+84 wt.% EG+ 10 wt.% PEG600+2 wt.% MBP	1560	6.8	466	A few concaves and cavities
The fourth	Same as the third but with carboxylic acid ester	1248	6.7	490	Many concaves and cavities

of the four electrolytes, their properties, and the morphologies of the anodic oxides.

4 Conclusions

(1) When pure aluminum is anodized at a constant current in non-corrosive capacitor working electrolytes that have been stored at high temperatures, inflection points appear in the voltage−time curves, the formation efficiency of anodic oxide is decreased, and nanopores can be found in the original dense films of anodic alumina.

(2) The electrolytes are still neutral after HTS, but the carboxylate and EG in the electrolytes can easily react with esterification at high temperatures.

(3) Combining the electronic current theory and oxygen bubble mold effect, the generation of electronic current could increase in the anodizing process after the HTS of electrolytes. The slope of the curve reflects the formation efficiency of anodic oxides in the anodizing process. The inflection points in the curves are due to the generation of electronic current. The electronic current decreases the formation efficiency of anodic oxides and leads to oxygen gas evolution. Oxygen bubbles remaining within the anodic oxide film form the nanopores. It also proves that chemical or field-assisted dissolution has no contribution to the anodizing current and does not affect the formation efficiency of anodic oxides.

CRediT authorship contribution statement

Peng-ze LI: Review & editing, Investigation; **Yu ZHANG:** Writing − Original draft, Methodology; **Jia-zheng ZHANG:** Formal analysis; **Lin LIU:** Review & editing; **Shi-yi WANG:** Supervision; **Rui LIU:** Formal analysis, Validation; **Ye SONG:** Review & editing, Conceptualization; **Xu-fei ZHU:** Conceptualization, Project administration.

Declaration of competing interest

The authors declare that they have no known competing financial interests or personal relationships that could have appeared to influence the work reported in this paper.

Acknowledgments

This work was financially supported by the National Natural Science Foundation of China (Nos. 51777097, 51577093).

References

[1] LI Peng-ze, WANG Jin, LIU Lin, MA Juan-juan, NI Yi-lin, WANG Heng, SONG Ye. The effect of atmospheric pressure on the growth rate of TiO_2 nanotubes: Evidence against the field-assisted dissolution theory [J]. Electrochemistry Communications, 2021, 132: 107146.

[2] LI Cheng-yuan, LUO Kun, YAN Bo-wen, SUN Wei-min, JIANG Long-fei, LI Peng-ze, ZHANG Yu, WANG Shi-yi, YU Yuan-tian, ZHU Xu-fei, SONG Ye. Simulation of anodic current and optimization of the fitting equation and the fitting algorithm during constant voltage anodization [J]. The Journal of Physical Chemistry C, 2023, 127: 9707−9716.

[3] CAO Guo-jian, CUI Bo, WANG Wen-qi, TANG Guang-ze, FENG Yi-cheng, WANG Li-ping. Fabrication and photo-degradation properties of TiO_2 nanotubes on porous Ti by anodization [J]. Transactions of Nonferrous Metals Society of China, 2014, 24: 2581−2587.

[4] TANG Han-chun, ZHAO Da-peng, WAN Chang-jun, LI Xiao-song, JI Xiao-wei, TANG Jin-cheng, CAO Yuan-kui, LIU Yong. Influence of heterogeneous microstructures on anodization behavior and biocompatibility of Ti−15Zr alloy [J]. Transactions of Nonferrous Metals Society of China, 2023, 33: 2076−2089.

[5] WANG Xiao-ming, ZHANG Fu-qin. Influence of anions in phosphate and tetraborate electrolytes on the growth kinetics of microarc oxidation coatings on Ti6Al4V alloy [J]. Transactions of Nonferrous Metals Society of China, 2022, 32: 2243−2252.

[6] ZHOU Jian-hua, HE Jian-ping, ZHAO Gui-wang, ZHANG Chuan-xiang, ZHAO Ji-shuang, HU Huo-ping. Alumina nanostructures prepared by two-step anodization process [J]. Transactions of Nonferrous Metals Society of China, 2007, 17: 82−86.

[7] BAN Chao-lei, HE Ye-dong, SHAO Xin. Effect of citric acid on microstructure and electrochemical characteristics of high voltage anodized alumina film formed on etched Al foils [J]. Transactions of Nonferrous Metals Society of China, 2011, 21: 133−138.

[8] RUIZ-CLAVIJO A, CABALLERO-CALERO O, MARTIN-GONZALEZ M. Revisiting anodic alumina templates: From fabrication to applications [J]. Nanoscale, 2021, 13: 2227−2265.

[9] LECLERE D J, VELOTA A, SKELDON P, THOMPSON G E, BERGER S, KUNZE J, SCHMUKI P, HABAZAKI H, NAGATA S. Tracer investigation of pore formation in anodic titania [J]. Journal of The Electrochemical Society, 2008, 155: 487−494.

[10] SECKIN E, URGEN M. A kinetic model for determining morphology transitions and growth kinetics of titania nanotubes during anodization of titanium in ethylene glycol based electrolytes [J]. Surface and Coatings Technology, 2021, 409: 126840.

[11] SU Zi-xue, ZHOU Wu-zong. Formation mechanism of porous anodic aluminum and titanium oxides [J]. Advanced Materials, 2008, 20: 3663−3667.

[12] SU Zi-xue, ZHOU Wu-zong. Formation, morphology control and applications of anodic TiO_2 nanotube arrays [J]. Journal of Materials Chemistry, 2011, 21: 8955−8970.

[13] GARCIA-VERGARA S J, SKELDON P, THOMPSON G E, HABAZAKI H. A flow model of porous anodic film growth

on aluminum [J]. Electrochimica Acta, 2006, 52: 681−687.

[14] HOUSER J E, HEBERT K R. The role of viscous flow of oxide in the growth of self-ordered porous anodic alumina films [J]. Nature Materials, 2009, 8: 415−420.

[15] DENG Ping-ye, BAI Xin-de, CHEN Xiao-wen, FENG Qing-ling. Anodic oxidization of aluminum at high current densities and mechanism of film formation [J]. Journal of the Electrochemical Society, 2004, 151: 284−289.

[16] ZHU Xu-fei, SONG Ye, LIU Lin, WANG Chen-yu, ZHENG Jie, JIA Hong-bing, WANG Xin-long. Electronic currents and the formation of nanopores in porous anodic alumina [J]. Nanotechnology, 2009, 20: 475303.

[17] ALBELLA J M, MONTERO I, MARTINEZ-DUART J M. A theory of avalanche breakdown during anodic oxidation [J]. Electrochimica Acta, 1987, 32: 255−258.

[18] GONG Tian-le, LI Cheng-yuan, LI Xin, YUE Hang-yu, ZHU Xu-fei, ZHAO Zi-yu, LV Ren-quan, ZHU Jun-wu. Evidence of oxygen bubbles forming nanotube embryos in porous anodic oxides [J]. Nanoscale Advances, 2021, 3: 4659−4668.

[19] HASEGAWA K, TSUZAKI K, NISHIZAWA S. DC-bias-voltage dependence of degradation of aluminum electrolytic capacitors [J]. Microelectronics Reliability, 2018, 83: 115−118.

[20] JIA Ming, HU Xiao-yu, LIU Jin, LIU Ye-xiang, AI Liang. Molecular adsorption at electrolyte/α-Al_2O_3 interface of aluminum electrolytic capacitor revealed by sum frequency vibrational spectroscopy [J]. The Journal of Chemical Physics, 2017, 146: 194706.

[21] ROMERO J, AZARIAN M H, PECHT M. Reliability analysis of multilayer polymer aluminum electrolytic capacitors [J]. Microelectronics Reliability, 2020, 112: 113725.

[22] LI Y, SHIMADA H, SAKAIRI M, SHIGYO K, TAKAHASHI H, SEO M. Formation and breakdown of anodic oxide films on aluminum in boric acid/borate solutions [J]. Journal of the Electrochemical Society, 1997, 144: 866−876.

[23] MERCIER D, van OVERMEERE Q, SANTORO R, PROOST J. In-situ optical emission spectrometry during galvanostatic aluminum anodising [J]. Electrochimica Acta, 2011, 56: 1329−1336.

[24] van OVERMEERE Q, PROOST J. Stress-induced breakdown during galvanostatic anodising of zirconium [J]. Electrochimica Acta, 2010, 55: 4653−4660.

[25] VRUBLEVSKY I, JAGMINAS A, SCHRECKENBACH J, GOEDEL W A. Electronic properties of electrolyte/anodic alumina junction during porous anodizing [J]. Applied Surface Science, 2007, 253: 4680−4687.

[26] ZHU Xu-fei, HAN Hua, SONG Ye, MA Hong-tu, QI Wei-xing, LU Chao, XU Chen. Forming efficiency of porous anodic oxide and formation mechanism of nanopores [J]. Acta Physica Sinica, 2012, 61: 228202.

[27] OH J H, THOMPSON C V. The role of electric field in pore formation during aluminum anodization [J]. Electrochimica Acta, 2011, 56: 4044−4051.

[28] BARON-WIECHEC A, BURKE M G, HASHIMOTO T, LIU H, SKELDON P, THOMPSON G E, HABAZAKI H, GANEM J J, VICKRIDGE I C. Tracer study of pore initiation in anodic alumina formed in phosphoric acid [J]. Electrochimica Acta, 2013, 113: 302−312.

[29] CAPRAZ O O, SHROTRIYA P, SKELDON P, THOMPSON G E, HEBERT K R. Role of oxide stress in the initial growth of self-organized porous aluminum oxide [J]. Electrochimica Acta, 2015, 167: 404−411.

[30] LI Xian-feng, CHEN Dong, CHEN Zhe, WU Yi, WANG Ming-liang, MA Nai-heng, WANG Hao-wei. Stability of nanopore formation in aluminum anodization in oxalic acid [J]. Transactions of Nonferrous Metals Society of China, 2012, 22(Suppl.): 105−109.

[31] LI Yi, LING Zhi-yuan, HU Xing, LIU Yi-sen, CHANG Yi. Investigation of intrinsic mechanisms of aluminium anodization processes by analyzing the current density [J]. RSC Advances, 2012, 2: 5164−5171.

[32] CHENG Yu-lin, XIE Huan-jun, CAO Jin-hui, CHENG Ying-liang. Effect of NaOH on plasma electrolytic oxidation of A356 aluminum alloy in moderately concentrated aluminate electrolyte [J]. Transactions of Nonferrous Metals Society of China, 2021, 31: 3677−3690.

致密型阳极氧化铝薄膜中纳米孔洞的形成机理

李鹏泽[1]，张 宇[1]，张嘉正[2]，刘 霖[2]，王诗意[1]，刘 瑞[1]，宋 晔[1]，朱绪飞[1]

1. 南京理工大学 软化学与功能材料教育部重点实验室，南京 210094；
2. 江苏海洋大学 环境与化学工程学院，连云港 222005

摘 要：为了探讨阳极氧化膜中纳米孔洞的形成机理，在无腐蚀性的电容器工作电解液中进行纯铝的恒流阳极氧化实验。对比实验发现，在 130 ℃高温储存 240 h 后的电解液中形成的阳极氧化膜中发现了纳米孔洞。由电压−时间曲线可知，纳米孔洞的形成是由于氧化膜形成效率的降低而不是电解液的腐蚀。傅里叶红外和紫外光谱分析结果表明，电解液中的羧酸盐和乙二醇在高温条件下很容易发生酯化反应。结合电子电流和氧气泡模具效应，电解液成分的改变会增大阳极氧化过程中的电子电流。电子电流会降低阳极氧化膜的形成效率，而伴随其产生的氧气泡会导致纳米孔洞的产生，即电子电流和氧气泡才是多孔氧化铝形成的先决条件，而非传统的场致助溶模型。

关键词：阳极氧化铝；形成机理；纳米孔洞；形成效率；电子电流；氧气泡

(Edited by Wei-ping CHEN)